Numerical/experimental study of the monotonic and cyclic viscoelastic/viscoplastic/fracture behavior of an epoxy resin

Rocha, I. B.C.M.; van der Meer, F. P.; Raijmaekers, S.; Lahuerta, F.; Nijssen, R. P.L.; Sluys, L. J.

DOI
10.1016/j.ijsolstr.2019.03.018

Publication date
2019

Document Version
Accepted author manuscript

Published in
International Journal of Solids and Structures

Numerical/Experimental study of the monotonic and cyclic viscoelastic/viscoplastic/fracture behavior of an epoxy resin

I. B. C. M. Rocha[1,2], F. P. van der Meer[2], S. Raijmaekers[1], F. Lahuerta[1], R. P. L. Nijssen[1], and L. J. Sluys[2]

[1]Knowledge Centre WMC, Kluisgat 5, 1771MV Wieringerwerf, The Netherlands
[2]Delft University of Technology, Faculty of Civil Engineering and Geosciences, P.O. Box 5048, 2600GA Delft, The Netherlands

Abstract

This paper investigates the viscoelastic/viscoplastic/fracture behavior of an epoxy resin. A state-of-the-art pressure-dependent elastoplastic constitutive model (Melro *et al.* (2013)) is expanded to include viscoelasticity, viscoplasticity and a modified damage formulation with linear softening and shrinking pressure-dependent fracture surface. A water plasticization model with a single degradation factor is proposed. A set of new quasi-static and fatigue experiments is used to calibrate the model and assess its predictive capabilities. The model correctly represents the rate dependent plasticity and fracture initiation behavior of the studied epoxy. The stiffness and strength degradations after plasticization are also accurately captured. The model is found to be less suitable in reproducing the measured loading-unloading behavior, which displayed strong nonlinearity in combination with limited permanent deformation. Nevertheless, reasonably accurate fatigue life predictions in the low-cycle regime are obtained.

Keywords: Viscoelasticity, Viscoplasticity, Fracture, Plasticization, Epoxy

1 Introduction

Epoxy resins are widely used in industrial applications, from paints, coatings and adhesives in its pure form to aerospace, marine and energy applications in the form of composite parts after combination with a range of synthetic or natural fibers. For the particular case of composites, the search for realistic material models capable of reproducing their complex mechanical behavior becomes more and more urgent. In this regard, multiscale approaches, in which each constituent material is explicitly modeled, become interesting since complex nonlinear constitutive phenomena can be captured and upscaled without loss of generality. These multiscale techniques are particularly useful when devising ply-level failure criteria considering complex loading cases [1, 2] and modeling inherently microscopic physical and chemical processes caused by exposing the material to extreme environments [3, 4]. In such applications, employing high-fidelity models for each constituent material is of utmost importance.

Accurate constitutive modeling of epoxies and other polymers is complicated by the fact that their mechanical behavior is time- and temperature-dependent. Such viscous effects give rise to phenomena such as strain rate dependency [5], ratcheting [6] and stress relaxation [7]. Additionally, polymers are known to develop permanent strains through pressure-dependent plastic yielding [8] and, in the particular case of crosslinked thermosets, undergo rate-dependent brittle failure at relatively low strain levels [9, 10]. Finally, all of these material features are sensitive to

physical and chemical effects caused by water absorption [11, 12], physical aging [13], oxidation [14], among others. Therefore, despite the already large amount of literature on the subject, experimental and numerical efforts on polymer characterization often ignore such complex material aspects.

A number of authors opt for elastoplastic constitutive models with pressure-dependent yielding [1, 3] calibrated using experiments with fixed strain rate and temperature and therefore ignoring the aforementioned viscous material features. The use of such models to describe material failure in fatigue or during aging may therefore be unrealistic. Phenomenological corrections have been proposed in order to introduce such dependencies by scaling a reference yield surface depending on rate and temperature [15]. However, this approach becomes unsuitable in loading situations with continuously changing strain rate or in non-isothermal conditions.

A second class of models attempts to introduce a time scale to the plastic flow rate while keeping the original inviscid yield surface [10, 16, 17, 12, 18]. This approach is interesting for finite element implementation since it can build upon previously implemented inviscid models. However, the temperature dependence is still not captured.

A third option in which temperature dependency is also addressed involves using Eyring-type rate equations [19], which consider yielding as a thermomechanically activated process [20, 21, 5, 22]. This is usually combined with a hyperelastic model in order to capture orientation hardening at high strains [5].

Finally, a number of physically-based macromolecular constitutive models have been devised which take into account changes in polymer chain orientation after yielding [9, 23, 24, 25, 26, 27, 28, 29, 30, 31]. In these approaches, both strain and temperature dependencies as well as orientation hardening are captured and arise as a consequence of underlying macromolecular mechanisms, providing a strong physical basis for the models. However, a number of drawbacks remain for application of these models in the numerical analysis of highly cross-linked thermosetting polymers. Firstly, most of the models are constructed with thermoplastic polymers in mind, which are capable to attain significantly higher strain levels. Consequently, the models are seldom concerned with material failure through fracture, while for highly cross-linked epoxies fracture is indeed observed at relatively low strain levels. Secondly, the models usually assume that no plastic deformation occurs before the peak stress, while experiments in epoxy show the occurrence of pre-peak plasticity (see [9] for an adapted macromolecular model). Thirdly, the models are often formulated in terms of principal stretches and seldom provide tangent stiffness operator expressions (notable exceptions are [31, 32]), making their finite element implementation and use for micromechanical modeling of complex stress states a difficult task.

Regarding modeling of the cyclic response of polymers, multiple works are limited to accurately describing the stress-strain behavior after a small number of loading-unloading cycles [11, 10, 18]. In those works, the viscoelastic-viscoplastic material behavior is taken into account but no attempt is made to model material failure in fatigue. At the other end of the spectrum, a number of works focus on high-cycle fatigue failure by phenomenologically imposing the evolution of a continuum damage internal variable with the number of fatigue cycles while ignoring viscous contributions [33, 34]. However, experimental results by multiple authors [29, 6, 7] emphasize the occurrence of fatigue failure with little to no change in stiffness, particularly in the high-cycle regime, which invalidates the use of a damage variable. It is important to note that modulus measurements in fatigue are affected by viscoelastic contributions that relax over time and might be erroneously interpreted as modulus degradation, in particular for tests in the low-cycle regime. For materials showing such type of fatigue failure behavior, appropriate definitions for the onset and evolution of damage are needed while maintaining a correct description of their viscous behavior.

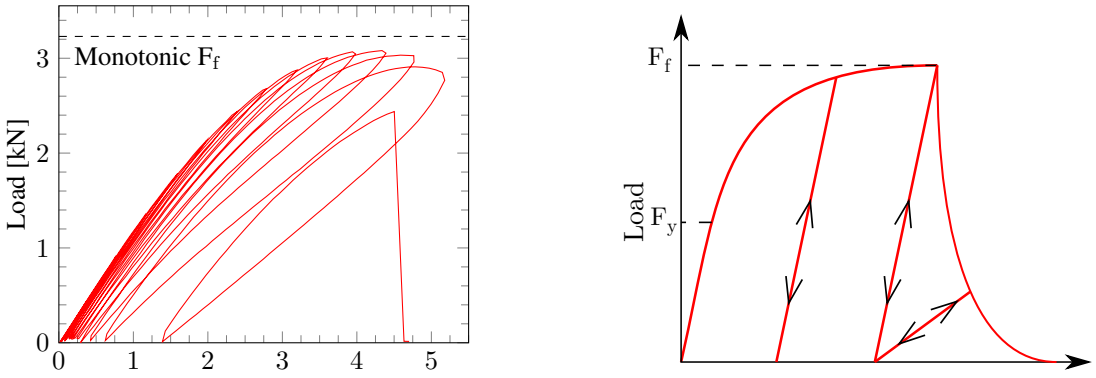

(a) Experimental response (b) Prediction using an E-P-D model

Figure 1: Material response in a loading-unloading scenario with increasing amplitude.

1.1 Experimental motivation

Figure 1 illustrates the shortcomings of using state-of-the-art elastoplastic-damage (E-P-D) formulations to model the cyclic behavior of the epoxy resin considered here. In a preliminary study, a material sample was subjected to a number of loading-unloading cycles at 1 mm/min with increasing displacement amplitudes until failure occurred. The resultant load-displacement curve can be seen in Figure 1a, while the expected material response using either the inviscid model by Melro *et al.* [1] or its rate-dependent variation proposed by Bai *et al.* [15] is shown in Figure 1b.

According to the model, the material behaves elastically up until the yield point F_y after which a hardening regime is observed until the fracture load F_f is reached. The model unloads and reloads elastically along the same path with a slope equal to the initial stiffness until damage is activated, at which point plasticity stops evolving and the stiffness gradually decreases until final failure. During reloading, the curve always meets its respective unloading point and the response returns to the curve for monotonic loading even if a rate-dependent yield surface is used [15], since the strain rate does not change throughout the test.

On the other hand, experimental unloading and reloading branches are nonlinear and do not follow the same path, with significant hysteresis (viscoelasticity). Upon reloading, the curve does not meet its original unloading point and further plastic strain develops (viscoplasticity). Finally, the specimen fails without ever reaching the monotonic failure load and without a gradual stiffness reduction, suggesting that fracture initiation is driven by plastic strain development and rapid crack propagation leading to brittle failure. Furthermore, subjecting the material to fatigue loads in the high-cycle regime leads to failure without any measurable loss of stiffness and after stabilization of ratcheting, suggesting that fracture initiation is not only affected by plastic strain development but also by phenomena occurring in the elastic regime.

Based on these preliminary investigations, a number of additional model ingredients may be proposed in order to improve the performance of conventional elastoplastic-damage models when dealing with time-dependent mechanical behavior while keeping as many of their original components as possible. Firstly, the observed hysteresis behavior can be captured by adding a time-dependent stiffness contribution to the existing elasticity formulation. Secondly, since permanent strains develop gradually under cyclic loading, plastic strain development must be retarded by allowing stresses to temporarily surpass the original yield surface. Finally, the existing damage formulation must be adjusted in order to allow for fracture initiation at load levels lower than the original fracture load by introducing a fracture surface shrink driven by both viscoelastic and viscoplastic mechanisms.

1.2 Outline of the study

In this paper, the state-of-the-art pressure-dependent elastoplastic formulation presented by Melro *et al*. [1] is expanded into a viscoelastic-viscoplastic-damage (VE-VP-D) model. The modified model can in turn be used in isolation or to provide more realistic predictions of the mechanical behaviour of composite materials subjected to monotonic or cyclic loadings through micromechanical modeling.

Viscoelasticity is incorporated through a series of springs and dashpots. Viscoplasticity is modeled through a Perzyna-type formulation. Fracture is modeled by a thermodynamically consistent damage model with linear softening and a fracture surface that shrinks as energy is dissipated. Finally, the mechanical model is complemented by a damage model with a single degradation factor in order to take into account changes in polymer behavior after moisture absorption. The formulations are presented in a way that facilitates their implementation in a finite element framework. The model is calibrated using an original series of monotonic and cyclic experiments on pure resin specimens both dry and after being saturated in water at $50\,^{\circ}\mathrm{C}$. After calibration, the model is used to predict the rate-dependent response of the water-saturated polymer and its behavior during loading-unloading and fatigue tests. The model performance is assessed by comparing these predictions with validation experiments.

2 Model formulation

2.1 Mathematical notation

In this work, both index notation and matrix notation will be used to represent tensors and vectors. When index notation is used, the indices i, j, k, l range from one to the number of spatial dimensions of the problem being solved. In products between two entities in index notation, summation over repeated indices is implied. In matrix notation, vectors are represented by boldfaced lower-case symbols while matrices are given by boldfaced upper-case symbols. When representing stresses and strains in matrix notation, the use of Voigt notation is implied.

2.2 Rheological model

The present model can be schematically represented by the rheological model of Figure 2. For a given applied stress, the strain response is decomposed into elastic and plastic parts. The elastic behavior is represented by a parallel chain of Maxwell elements with springs and dashpots to which a long-term spring is added. The plastic behavior is represented by a sliding element on which the stress cannot be higher than the yield stress σ_{y}. By adding a dashpot element in parallel with the sliding element, an overstress is allowed to develop resulting in viscoplastic behavior. Finally, damage is enforced by degrading the resultant effective stress $\widetilde{\sigma}$.

In the following sections, each model component will be formulated and expressions for stress update and tangent stiffness will be provided in order to facilitate their implementation in general finite element codes.

2.3 Viscoelasticity

In the model, an additive decomposition of strain in elastic and plastic parts is considered:

$$\varepsilon_{ij} = \varepsilon_{ij}^{\mathrm{e}} + \varepsilon_{ij}^{\mathrm{p}} \tag{1}$$

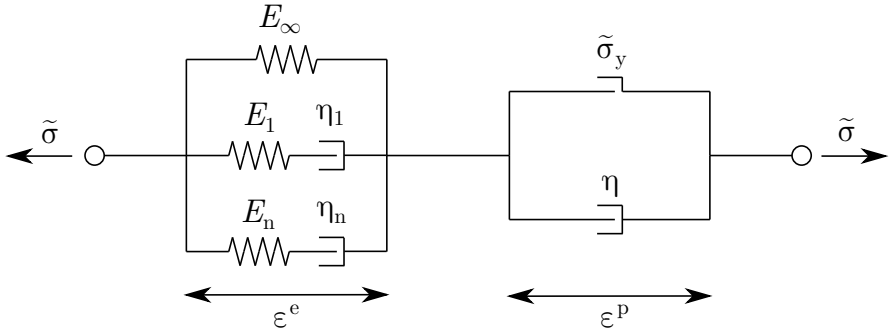

Figure 2: Schematic representation of the VE/VP/D model.

The viscoelastic stress is computed in integral form by applying the Boltzmann superposition principle [16]:

$$\sigma_{ij}(t) = D^{\infty}_{ijkl}\varepsilon^{\mathrm{e}}_{kl}(t) + \int_0^t D^{\mathrm{ve}}_{ijkl}(t-\tilde{t})\frac{\partial \varepsilon^{\mathrm{e}}_{kl}(\tilde{t})}{\partial \tilde{t}}d\tilde{t} \tag{2}$$

where the long-term and viscous contributions are explicitly separated. The long-term elastic stiffness D^{∞}_{ijkl} is given by:

$$D^{\infty}_{ijkl} = G_\infty(\delta_{ij}\delta_{kl} + \delta_{il}\delta_{jk}) + \left(K_\infty - \frac{2}{3}G_\infty\right)\delta_{ij}\delta_{kl} \tag{3}$$

where G_∞ and K_∞ are the long term shear and bulk modulus, respectively. It is important to note that the response of this back-bone elastic solid is time-independent and is therefore taken out of the integral of Eq. (2).

The viscoelastic contribution has a similar form but is now composed of time-dependent stiffnesses:

$$D^{\mathrm{ve}}_{ijkl}(t) = G_{\mathrm{ve}}(t)(\delta_{ij}\delta_{kl} + \delta_{il}\delta_{jk}) + \left(K_{\mathrm{ve}}(t) - \frac{2}{3}G_{\mathrm{ve}}(t)\right)\delta_{ij}\delta_{kl} \tag{4}$$

where G_{ve} and K_{ve} are the stiffnesses of the Maxwell elements of Figure 2 and can be expressed as a Prony series of n_r bulk elements and n_s shear elements:

$$K_{\mathrm{ve}}(t) = \sum_{r=1}^{n_r} K_r \exp\left(-\frac{t}{k_r}\right) \qquad G_{\mathrm{ve}}(t) = \sum_{s=1}^{n_s} G_s \exp\left(-\frac{t}{g_s}\right) \tag{5}$$

where K_r, G_s, k_r and g_s are bulk and shear stiffnesses and relaxation times, respectively.

In order to avoid performing the time integration of Eq. (2) at every time step and thus having to store the whole strain history of every material point, the stress update can be represented in a time discrete manner. Following the development in Haouala and Doghri [16], Eq. (2) becomes:

$$\sigma_{ij}(t_{n+1}) = D^{\infty}_{ijkl}\varepsilon^{\mathrm{e}}_{kl}(t_{n+1}) + \sum_{r=1}^{n_r} p^{\mathrm{ve}}_r(t_{n+1})\delta_{ij} + \sum_{s=1}^{n_s} S^{\mathrm{ve}}_{ij,s}(t_{n+1}) \tag{6}$$

where the deviatoric and hydrostatic viscoelastic stress contributions S^{ve}_{ij} and p^{ve} of each Prony element are given by:

$$p^{\mathrm{ve}}_r(t_{n+1}) = \exp\left(\frac{-\Delta t}{k_r}\right)p^{\mathrm{ve}}_r(t_n) + K_r\left[1-\exp\left(\frac{-\Delta t}{k_r}\right)\right]\frac{k_r}{\Delta t}\left(\varepsilon^{\mathrm{e}}_{\mathrm{v}}(t_{n+1}) - \varepsilon^{\mathrm{e}}_{\mathrm{v}}(t_n)\right) \tag{7}$$

$$S^{\mathrm{ve}}_{ij,s}(t_{n+1}) = \exp\left(\frac{-\Delta t}{g_s}\right)S^{\mathrm{ve}}_{ij,s}(t_n) + 2G_s\left[1-\exp\left(\frac{-\Delta t}{g_s}\right)\right]\frac{g_s}{\Delta t}\left(\varepsilon^{\mathrm{e}}_{ij,\mathrm{d}}(t_{n+1}) - \varepsilon^{\mathrm{e}}_{ij,\mathrm{d}}(t_n)\right) \tag{8}$$

where $\Delta t = t_{n+1} - t_n$ is the time step, $\varepsilon_{\mathrm{v}} = \varepsilon_{kk}$ is the volumetric part of the strain and $\varepsilon_{ij,\mathrm{d}} = \varepsilon_{ij} - 1/3\varepsilon_{\mathrm{v}}\delta_{ij}$ is the deviatoric part. In discrete form, only information about the previous converged time step t_n has to be stored. Finally, the total elastic stiffness can be found by substituting Eqs. (7) and (8) into Eq. (6):

$$D^{\mathrm{e}}_{ijkl}(t_{n+1}) = D^{\infty}_{ijkl} + D^{\mathrm{ve}}_{ijkl}(\Delta t) \tag{9}$$

2.4 Viscoplasticity

In contrast with the stress update for viscoelasticity, an iterative procedure is necessary in order to compute the stresses in the viscoplastic regime. At first, it is assumed that the increment of strain is viscoelastic and a trial stress is computed. By explicitly isolating historical terms from terms that operate on the current strain increment in Eq. (6), the trial stress is computed as:

$$\sigma^{\mathrm{tr}}_{ij} = D^{\infty}_{ijkl}\big(\varepsilon_{kl}(t_{n+1}) - \varepsilon^{\mathrm{p}}_{kl}(t_n)\big) + D^{\mathrm{ve}}_{ijkl}\big(\varepsilon_{kl}(t_{n+1}) - \varepsilon^{\mathrm{p}}_{kl}(t_n) - \varepsilon^{\mathrm{e}}_{kl}(t_n)\big) + \sigma^{\mathrm{hist}}_{ij}(t_n) \tag{10}$$

If no further plastic strain is developed, the computed trial stress is correct and the update is completed by updating the historical stresses of Eqs. (7) and (8). However, if the amount of plastic strain changes, the stresses must be corrected:

$$\sigma_{ij} = \sigma^{\mathrm{tr}}_{ij} - (D^{\infty}_{ijkl} + D^{\mathrm{ve}}_{ijkl})\Delta\varepsilon^{\mathrm{p}}_{kl} \tag{11}$$

and the historical stresses must be updated using the correct value for the elastic strain.

The yield surface adopted in this model is the one proposed by Melro et al. [1]:

$$f_{\mathrm{p}}(\boldsymbol{\sigma}, \varepsilon^{\mathrm{p}}_{\mathrm{eq}}) = 6J_2 + 2I_1\big(\sigma_c - \sigma_t\big) - 2\sigma_c\sigma_t \tag{12}$$

where σ_t and σ_c are the yield stresses in tension and compression, respectively, $I_1 = \sigma_{kk}$ is the first stress invariant and $J_2 = \frac{1}{2}S_{ij}S_{ij}$ is the second invariant of the deviatoric stress.

The hardening behavior is a consequence of the evolution of the yield stresses σ_t and σ_c, which are functions of the equivalent plastic strain:

$$\Delta\varepsilon^{\mathrm{p}}_{\mathrm{eq}} = \sqrt{\frac{1}{1+2\nu^2_{\mathrm{p}}}\Delta\varepsilon^{\mathrm{p}}_{ij}\Delta\varepsilon^{\mathrm{p}}_{ij}} \;\Rightarrow\; \sigma_t = \sigma_t(\varepsilon^{\mathrm{p}}_{\mathrm{eq}}),\ \sigma_c = \sigma_c(\varepsilon^{\mathrm{p}}_{\mathrm{eq}}) \tag{13}$$

where ν_p is the plastic Poisson ratio and the yield stresses are given by functions of equivalent plastic strain that can take any form. The variation in plastic strains is computed through a non-associative flow rule:

$$\Delta\varepsilon^{p}_{ij} = \Delta\gamma\left(3S_{ij} + \frac{2}{9}\alpha I_1\delta_{ij}\right) \tag{14}$$

where γ is the plastic multiplier, the expression in parentheses is the plastic flow direction, and α is:

$$\alpha = \frac{9}{2}\frac{1-2\nu_p}{1+\nu_p} \tag{15}$$

The choice for non-associative plasticity is related to the pressure dependency of the model and is done in order to avoid the occurrence of spurious volumetric plastic strains [1].

A viscous time scale is introduced in the model by relaxing the classic Kuhn-Tucker conditions on the yield function and allowing it to attain positive values. This effectively delays the development of plastic strains and allows for the development of an overstress above the yield surface. In this work, the Perzyna-type formulation used in [16] is modified for the yield surface of Eq. (12) and dictates the evolution of the plastic multiplier:

$$\Delta\gamma = \begin{cases} \frac{\Delta t}{\eta_{\mathrm{p}}}\left(\frac{f_{\mathrm{p}}}{\sigma^0_{\mathrm{t}}\sigma^0_{\mathrm{c}}}\right)^{m_{\mathrm{p}}}, & \text{if } f > 0 \\ 0, & \text{if } f \leq 0 \end{cases} \tag{16}$$

where the time discrete expression is obtained through a backward Euler scheme [16], the superscript 0 indicates yield stress values for $\varepsilon^{\mathrm{p}}_{\mathrm{eq}} = 0$, and η_{p} and m_{p} are the viscoplastic modulus and exponent, respectively.

With the definition of the flow rule, the stresses of Eq. (11) may be written as:

$$\sigma_{ij} = \frac{S^{\mathrm{tr}}_{ij}}{\zeta_s} + \frac{I^{\mathrm{tr}}_1 \delta_{ij}}{3\zeta_p} \tag{17}$$

where the factors ζ_s and ζ_p are:

$$\zeta_s = 1 + 6\big(G_\infty + G_{\mathrm{ve}}(\Delta t)\big)\Delta\gamma \;\; \Rightarrow \zeta_s = 1 + 6\widehat{G}\Delta\gamma \tag{18}$$

$$\zeta_p = 1 + 2\big(K_\infty + K_{\mathrm{ve}}(\Delta t)\big)\alpha\Delta\gamma \;\; \Rightarrow \zeta_p = 1 + 2\widehat{K}\alpha\Delta\gamma \tag{19}$$

Substituting Eq. (17) into the equivalent plastic strain expression of Eq. (13) through Eq. 14 and into the yield surface of Eq. (12), Eq. (16) becomes a function of $\Delta\gamma$ only and can be solved iteratively using Newton's method:

$$\Phi(\Delta\gamma) = \frac{\Delta t}{\eta_{\mathrm{p}}}(\Delta\gamma)\left(\frac{f_{\mathrm{p}}}{\sigma^0_{\mathrm{t}}\sigma^0_{\mathrm{c}}}\right)^{m_{\mathrm{p}}} - \Delta\gamma = 0 \tag{20}$$

In order to accelerate convergence, it is also necessary to compute the derivative of Eq. (20) with respect to $\Delta\gamma$. This derivation is shown in A. Finally, the derivation of the consistent tangent stiffness matrix for the viscoplastic part of the model is shown in B.

2.5 Damage

The formulation for the damage model starts with the definition of a measure of material free energy [35, 10]:

$$\Psi = (1-d)\left[\frac{1}{2}\int_0^t\int_0^t \frac{\partial\varepsilon^{\mathrm{e}}_{ij}(\bar{t})}{\partial\bar{t}} D^{\mathrm{e}}_{ijkl}(2t-\bar{t}-\tilde{t})\frac{\partial\varepsilon^{\mathrm{e}}_{kl}(\tilde{t})}{\partial\tilde{t}}d\bar{t}d\tilde{t}\right] + \Psi^{\mathrm{h}} \tag{21}$$

where $0 \leq d \leq 1$ is the single damage variable adopted in this work and the plastic harderning energy contribution Ψ^{h} has been ommited for compactness. It is worth mentioning that damage evolution is not linked to the development of plastic strains, as adopted by Krairi and Doghri [10], but rather evolves independently, similar to the approach adopted by Simo and Ju [35] and Melro *et al.* [1].

For this particular definition of free energy, the term within brackets can be readily identified as the thermodynamic force $Y = -\partial\Psi/\partial d$, and Eq. (21) may be rewritten as:

$$\Psi = (1-d)Y + \Psi^{\mathrm{h}} \tag{22}$$

In order to impose the second law of thermodynamics and assure that damage is an energetically irreversible process, the Clausius-Duhem inequality for the isothermal case is imposed:

$$\Xi = \sigma_{ij}\dot{\varepsilon}_{ij} - \dot{\Psi} \geq 0 \tag{23}$$

where Ξ is the mechanical energy dissipation. Following the derivation by Krairi and Doghri [10], the total derivative of the energy can be given by:

$$\begin{aligned}\dot{\Psi} = (1-d)\Bigg[&\frac{1}{2}\int_0^t\int_0^t \frac{\partial\varepsilon^{\mathrm{e}}_{ij}(\bar{t})}{\partial\bar{t}}\frac{\partial D^{\mathrm{e}}_{ijkl}(2t-\bar{t}-\tilde{t})}{\partial t}\frac{\partial\varepsilon^{\mathrm{e}}_{kl}(\tilde{t})}{\partial\tilde{t}}d\bar{t}d\tilde{t} \\ &+ \frac{\partial\varepsilon^{\mathrm{e}}_{ij}}{\partial t}\int_0^t D^{\mathrm{e}}_{ijkl}(t-\tilde{t})\frac{\partial\varepsilon^{\mathrm{e}}_{kl}(\tilde{t})}{\partial\tilde{t}}d\tilde{t}\Bigg] - Y\dot{d} + \dot{\Psi}^{\mathrm{h}}\end{aligned} \tag{24}$$

Substituting Eq. (24) into the inequality of Eq. (23) and splitting the strains in elastic and plastic parts as shown in Eq. (1), the damaged stress-strain relationship is recovered:

$$\sigma_{ij} = (1-d)\int_0^t D^{\mathrm{e}}_{ijkl}(t-\tilde{t})\frac{\partial \varepsilon^{\mathrm{e}}_{kl}(\tilde{t})}{\partial \tilde{t}}d\tilde{t} \tag{25}$$

and the dissipation now reads:

$$\Xi = Y\dot{d} + (1-d)\Xi^{\mathrm{ve}} + \Xi^{\mathrm{p}} \tag{26}$$

where Ξ^{p} is the plastic dissipation:

$$\Xi^{\mathrm{p}} = \sigma_{ij}\dot{\varepsilon}^{\mathrm{p}}_{ij} - \dot{\Psi}^{\mathrm{h}} \tag{27}$$

and Ξ^{ve} is the viscoelastic dissipation, given by:

$$\Xi^{\mathrm{ve}} = -\frac{1}{2}\int_0^t\int_0^t \frac{\partial \varepsilon^{\mathrm{e}}_{ij}(\bar{t})}{\partial \bar{t}}\frac{\partial D^{\mathrm{e}}_{ijkl}(2t-\bar{t}-\tilde{t})}{\partial t}\frac{\partial \varepsilon^{\mathrm{e}}_{kl}(\tilde{t})}{\partial \tilde{t}}d\bar{t}d\tilde{t} \tag{28}$$

Adopting the concept of effective stress proposed by Simo and Ju [35], stresses in the undamaged portion of the material can be written as:

$$\widetilde{\sigma}_{ij} = \frac{\sigma_{ij}}{1-d} \tag{29}$$

Using this definition and Eqs. (6) and (25), the thermodynamic force and viscoelastic dissipation can be expressed in terms of effective stress as [10]:

$$Y = \frac{\widetilde{S}^{\infty}_{ij}\widetilde{S}^{\infty}_{ij}}{4G_\infty} + \frac{(\tilde{p}^{\infty})^2}{2K_\infty} + \sum_{s=1}^{n_s}\frac{\widetilde{S}^{\mathrm{ve}}_{ij,s}\widetilde{S}^{\mathrm{ve}}_{ij,s}}{4G_s} + \sum_{r=1}^{n_r}\frac{(\tilde{p}^{\mathrm{ve}}_r)^2}{2K_r} \tag{30}$$

$$\Xi^{\mathrm{ve}} = \sum_{s=1}^{n_s}\frac{\widetilde{S}^{\mathrm{ve}}_{ij,s}\widetilde{S}^{\mathrm{ve}}_{ij,s}}{2G_s g_s} + \sum_{r=1}^{n_r}\frac{(\tilde{p}^{\mathrm{ve}}_r)^2}{K_r k_r} \tag{31}$$

For numerical simulation purposes, the stress update of Eq. (25) is done in a time discrete manner in the same way as done in Eq. (6). The deviatoric and hydrostatic stresses used to compute Y and Ξ^{ve} are therefore the ones at time t_{n+1}.

In order to control the evolution of damage, an internal variable $r \in [1,\infty]$ is adopted to represent the size of a pressure-dependent paraboloidal fracture surface in effective stress space:

$$f_{\mathrm{d}}(\widetilde{\boldsymbol{\sigma}}, r) = \frac{3\widetilde{J}_2}{X_{\mathrm{c}}X_{\mathrm{t}}} + \frac{\widetilde{I}_1(X_{\mathrm{c}}-X_{\mathrm{t}})}{X_{\mathrm{c}}X_{\mathrm{t}}} - r \quad \Rightarrow \quad f_{\mathrm{d}}(\widetilde{\boldsymbol{\sigma}}, r) = \Lambda - r \tag{32}$$

which is similar to the yield surface of Eq. (12) but with the yield stresses substituted by the fracture strengths X_{c} and X_{t}.

In order to allow for rate-dependent damage initiation, the viscosity already included in the preceding viscoelastic/viscoplastic formulation is exploited by making the fracture surfaces X_{t} and X_{c} general functions of an accumulated energy measure Υ which allows them to shrink as the material dissipates energy:

$$X_{\mathrm{t}} = X_{\mathrm{t}}(\Upsilon) \qquad X_{\mathrm{c}} = X_{\mathrm{c}}(\Upsilon) \tag{33}$$

where Υ includes the dissipated energy and the energy stored by hardening:

$$\Upsilon(t) = \int_{\tau=0}^{t}\left[\Xi^{\mathrm{ve}}(\tau) + \sigma_{ij}(\tau)\dot{\varepsilon}^{\mathrm{p}}_{ij}(\tau)\right]\mathrm{d}\tau \tag{34}$$

which allows for damage initiation both in a quasi-static or low-cycle fatigue scenarios (dominated by Ξ^{p}) as well as in the high-cycle fatigue regime (dominated by Ξ^{ve}).

As this shrink is driven by both VE and VP contributions, the present formulation is a departure from the classic Chaboche-Lemaitre coupled plasticity-damage models that explicitly consider damage as a function of plastic strain [36, 10]. The advantage of the proposed approach lies in allowing for fracture initiation even after the backbone plastic yield surface is reached, for instance after ratcheting stabilizes during a fatigue test [6]. Such a link between damage activation and dissipated energy has also been put forward in literature both for quasi-static loading [10] and for fatigue [6, 7]. After damage initiates, the fracture surface is kept constant in order to control the amount of energy that is dissipated during damage development.

Using the classic loading-unloading conditions $\dot{r} \geq 0;\ f_{\mathrm{d}} \leq 0;\ \dot{r} f_{\mathrm{d}} = 0$, the value of r can be explicitly obtained:

$$r_{t_{n+1}} = \max\left\{1, \max_{0 \leq t \leq t_{n+1}} \Lambda_t\right\} \tag{35}$$

It is worth mentioning that, in contrast with the plasticity-coupled damage evolution models used by Krairi and Doghri [10] and Zhu and Sun [18], damage and plasticity evolve independently in the present formulation.

Having defined an evolution law for the internal variable r, it is necessary to relate it to damage variable d. Since it is often difficult to experimentally obtain fracture properties using axially loaded specimens due to structural instabilities such as necking [9] and kinetic energy dissipation due to rapid crack propagation, a damage evolution law with linear softening based on an uniaxial tensile test is adopted for simplicity [37]:

$$d = \begin{cases} \dfrac{\widetilde{\sigma}_{\mathrm{f}}(\widetilde{\sigma}_{\mathrm{eq}} - \widetilde{\sigma}_0)}{\widetilde{\sigma}_{\mathrm{eq}}(\widetilde{\sigma}_{\mathrm{f}} - \widetilde{\sigma}_0)}, & \widetilde{\sigma}_{\mathrm{eq}} \leq \widetilde{\sigma}_{\mathrm{f}} \\ 1, & \widetilde{\sigma}_{\mathrm{eq}} > \widetilde{\sigma}_{\mathrm{f}} \end{cases} \tag{36}$$

where $\widetilde{\sigma}_0$ and $\widetilde{\sigma}_{\mathrm{f}}$ are the effective stress levels at the onset of damage and at complete failure, respectively:

$$\widetilde{\sigma}_0 = X_{\mathrm{t}} \qquad \widetilde{\sigma}_{\mathrm{f}} = \frac{2G^* \widehat{E}}{l_{\mathrm{e}} X_{\mathrm{t}}} \tag{37}$$

with $\widetilde{\sigma}_{\mathrm{eq}}$ being an equivalent stress measure that allows the treatment of multiaxial stress states, $\widehat{E}$ the instantaneous Young's modulus computed from $\widehat{K}$ and $\widehat{G}$ and G^* an energy parameter related to the fracture energy G_{c} which is regularized using the finite element characteristic length l_{e} according to Bažant's crack band model [38]. Depending on the element type, l_{e} can be computed as:

$$l_{\mathrm{e}}^{\mathrm{2D}} = \frac{6}{\pi \sqrt[4]{3}} \sqrt{A_{\mathrm{e}}} \qquad l_{\mathrm{e}}^{\mathrm{3D}} = \sqrt[3]{V_{\mathrm{e}}} \tag{38}$$

where A_{e} and V_{e} are the element area and volume, respectively. These are computed as the sum of the integration weights of each element in a mesh, yielding the area in case the element is 2D or the volume in case a 3D element is used. Finally, the expression for $\widetilde{\sigma}_{\mathrm{eq}}$ can be found by evaluating $\widetilde{I}_1$ and $\widetilde{J}_2$ for an uniaxial stress state, inserting them into Eq. (32) and imposing the loading condition $f_{\mathrm{d}} = 0$:

$$\widetilde{\sigma}_{\mathrm{eq}} = \frac{X_{\mathrm{t}} - X_{\mathrm{c}} + \sqrt{(X_{\mathrm{t}} - X_{\mathrm{c}})^2 + 4 X_{\mathrm{c}} X_{\mathrm{t}} r}}{2} \tag{39}$$

It is important to acknowledge that adopting the free energy measure of Eq. (21) implicitly assumes that the Poisson's ratio will remain unchanged, leading to the aforementioned discrepancy between G^* and G_{c}. Furthermore, keeping a constant ratio may lead to undesired spurious hardening when a band of elements is softening while being constrained by bands of elastically

unloading elements. For a non-viscous model that accounts for this effect, the reader is referred to [37]. Similar to the model by Melro *et al.* [1], plasticity is deactivated after initiation of damage in order to guarantee that the energy dissipated during the whole fracture process (*i.e.* up until the damage reaches $d = 1$) is equal to the input fracture toughness G^*.

After updating r, the damage variable d and the stresses can be computed using Eqs. (36) and (25), respectively. In a numerical analysis context, it is also important to compute the algorithmic tangent stiffness matrix, the derivation of which is shown in C.

2.6 Water concentration dependency

In this work, the mechanical models of the preceding sections are complemented by a simple model for representing the effects of plasticization after water absorption on the mechanical properties of epoxy resins. This is of particular importance when accurate predictions of long-term material performance during service are sought. Experimental evidence suggests that physical processes such as plasticization promote significant changes in stiffness and strength after water absorption [39, 3, 12]. In the present formulation, such changes are represented by a single degradation factor d_{w}:

$$d_{\mathrm{w}} = \frac{d_{\mathrm{w}}^{\infty}}{c_{\infty}} c \tag{40}$$

where a linear dependency on the water concentration c is assumed and c_{∞} and d_{w}^{∞} are the concentration and the degradation level at saturation, respectively.

The degradation factor is then used to modify the properties as follows:

$$\widehat{K}_{\mathrm{w}} = (1 - d_{\mathrm{w}})\widehat{K}, \;\; \widehat{G}_{\mathrm{w}} = (1 - d_{\mathrm{w}})\widehat{G} \tag{41}$$

$$\sigma_{\mathrm{c}}^{\mathrm{w}} = (1 - d_{\mathrm{w}})\sigma_{\mathrm{c}}, \;\; \sigma_{\mathrm{t}}^{\mathrm{w}} = (1 - d_{\mathrm{w}})\sigma_{\mathrm{t}} \tag{42}$$

$$X_{\mathrm{c}}^{\mathrm{w}} = (1 - d_{\mathrm{w}})X_{\mathrm{c}}, \;\; X_{\mathrm{t}}^{\mathrm{w}} = (1 - d_{\mathrm{w}})X_{\mathrm{t}}, \;\; G_{\mathrm{w}}^{*} = (1 - d_{\mathrm{w}})^2 G^{*} \tag{43}$$

where the viscoelastic relaxation times and the viscoplastic modulus and exponent are assumed to remain constant. The validity of such simplifications will be assessed in the next section. It is important to note that, in contrast with the damage formulation introduced in Section 2.5, the evolution of d_{w} is not irreversible and complete property recovery can be achieved through drying.

3 Experiments

3.1 Manufacturing and conditioning

The epoxy resin considered in this work is the Momentive EPIKOTE RIMR 135 / EPIKURE RIMH 1366, with a ratio between monomer and hardener of 100:30 in weight. Panels with a thickness of 3 mm were manufactured through vaccuum infusion molding (Figure 3a), with a curing cycle consisting of 2 h at 30°C, 5 h at 50°C and 10 h at 70°C.

Specimens were cut from the panels using a CNC milling machine in a custom-tailored short dog-bone shape that induces a stress concentration at a single point at mid-length (Figure 4). Inducing strain localization at the center of the specimen in contrast to having a longer gauge length reduces the influence of material imperfections on the fracture behavior of the material and limits the influence of necking on its yield behavior by hindering its formation and propagation along the length. It is important to note that necking (in tension) and barreling (in compression) are structural instabilities which do not represent intrinsic material behavior and therefore do not generate useful data for model calibration [9]. Beam-shaped specimens used for Dynamic Mechanical Analysis (DMA) tests were also extracted from the panels.

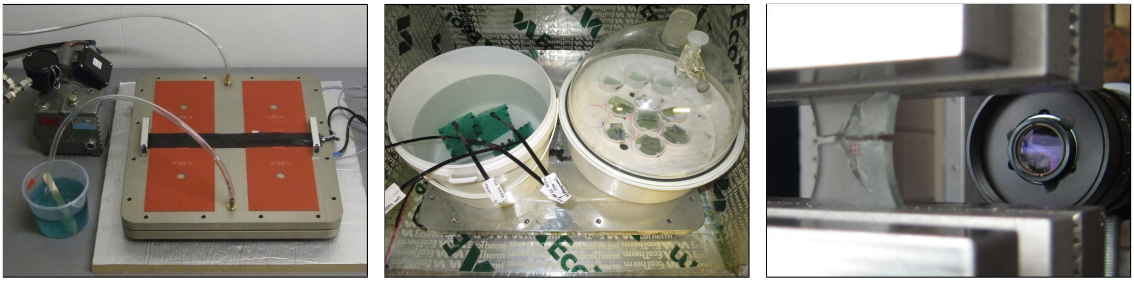

(a) Manufacturing (b) Conditioning (c) Testing

Figure 3: Experimental procedure workflow.

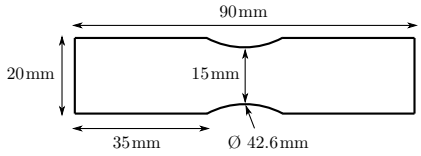

Figure 4: Planar dimensions of the specimens used for tension experiments (thickness is 3 mm).

After cutting, part of the specimens was kept in a desiccator at 50°C in vacuum until the time of testing in order to guarantee a moisture-free material state and achieve stabilization of molecular relaxation processes (physical aging) and post-curing [13], effectively creating a baseline material state with which results in aged samples will be compared. Another set of specimens was conditioned in demineralized water at 50°C (20°C lower than the saturated T_g [40]) and tested after saturation at a concentration level of 3.2%. The conditioning setups are shown in Figure 3b.

3.2 Mechanical tests

For calibration of the viscoelastic moduli and relaxation times, DMA tests were conducted using a Netzsch DMA 242 E Artemis apparatus. Dry and saturated prismatic samples (55 x 10 x 3 mm^3) were loaded in three-point bending with a deflection amplitude of 100 μm at multiple frequencies ranging from 0.1 Hz to 25 Hz, resulting in storage (E') and loss (E') moduli values as a function of frequency. The reported DMA results and calibrated viscoelastic properties were obtained using averaged measurements from two specimens.

Dry and saturated dog-bone specimens were tested in tension in an MTS universal test frame in displacement control at three different nominal rates (0.1 mm/min, 1 mm/min and 36 mm/min). Furthermore, dry specimens were tested in tension until failure with intermediate unloading branches and in stress-controlled fatigue with an R ratio of 0.1. For quasi-static and loading-unloading tests, two specimens were tested for each condition. For fatigue, four different stress levels were considered with 3 specimens being tested for each level. All tests were conducted at standard laboratory conditions (23°C, 50%RH). The dependency of resin properties on temperature will therefore not be treated in this work. For relevant investigations on the matter, the reader is referred to [9, 12].

Strain in the longitudinal direction was measured through micro video-extensometry by stamping an array of dots covering an area of 1.8 x 1.8 mm^2 at the center of the specimens and tracking their positions throughout the test using a camera equipped with a microscope lens (Figure 3c). Each frame from the resultant videos was then assigned a time stamp in sync with the load and displacement signals from the test frame. Finally, the relative distances between the dots at the edges of the tracked area were used to compute the engineering strain ε_x. Since the constitutive features of interest are located in the low strain regime and measurements after global softening (strain localization) occurs are not used for calibration, the use of engineering strains was considered a

reasonable approach.

3.3 Model calibration

3.3.1 Viscoelasticity and moisture dependency

Calibration of viscoelastic properties was performed following Miled [41]. The dynamic moduli obtained through DMA can be expressed as a function of the oscillatory frequency ω and the Prony moduli and relaxation times:

$$E'(\omega) = E_\infty + \sum_{i=1}^{n_\mathrm{i}} \frac{E_i \omega^2}{\frac{1}{\tau_i^2} + \omega^2} \tag{44}$$

$$E''(\omega) = \sum_{i=1}^{n_\mathrm{i}} \frac{E_i \frac{\omega}{\tau_i}}{\frac{1}{\tau_i^2} + \omega^2} \tag{45}$$

The value for E_∞ and for the viscoelastic moduli E_i and relaxation times τ_i were fit to the data through a nonlinear least squares procedure. Finally, bulk and shear values were obtained under the assumption of a constant Poisson's ratio [10, 16, 41]:

$$G_\infty = \frac{E_\infty}{2(1+\nu)} \qquad G_i = \frac{E_i}{2(1+\nu)} \qquad g_i = \frac{\tau_i E_i}{G_i} \tag{46}$$

$$K_\infty = \frac{E_\infty}{3(1-2\nu)} \qquad K_i = \frac{E_i}{3(1-2\nu)} \qquad k_i = \frac{\tau_i E_i}{K_i} \tag{47}$$

with $\nu = 0.37$ obtained in previous experiments on the same material system [40].

Figure 5 shows the obtained values for storage (E') and loss (E") moduli of dry DMA samples, with the lines representing the best attained fit. The resultant properties, comprising 4 Prony elements, are shown in Table 1. Since the value for E_∞ was also obtained from the same fitting procedure, the resultant optimization problem features a large number of local minima. Therefore, the least squares procedure was performed multiple times starting from random values for the moduli and relaxation times until a final fit was chosen which featured good agreement in terms of loss modulus without significantly sacrificing precision in terms of storage modulus. The fitted model can describe the viscoelastic behavior reasonably well, with small deviations in storage modulus for frequencies between 0.1 Hz and 1 Hz and in loss modulus between 1 Hz and 4 Hz. The fitting procedure was also performed with a higher number of Prony elements, but the quality of the fit did not improve further.

With this set of dry VE properties, another fitting procedure was performed in order to determine the moisture degradation factor d_w^∞ using DMA results from saturated samples. The results can be seen in Figure 6. For the present material system, a value of $d_\mathrm{w}^\infty = 0.14$ was found to correctly represent the material behavior after saturation without having to obtain another complete set of VE properties. It can be seen, however, that differences in loss moduli are slightly higher than for the dry case, suggesting that plasticization not only promotes stiffness degradation but also lead to a slightly more pronounced viscoelastic behavior. With the obtained degradation factor, no additional calibration is necessary in order to describe the behavior of the saturated resin.

3.3.2 Viscoplasticity

For calibration of the viscoplastic properties, the model of Section 2 was implemented in an in-house finite element code using the Jem/Jive C++ library [42]. In order to obtain an accurate stress value at the center of the specimen from the force signal of the load cell, the complete geometry

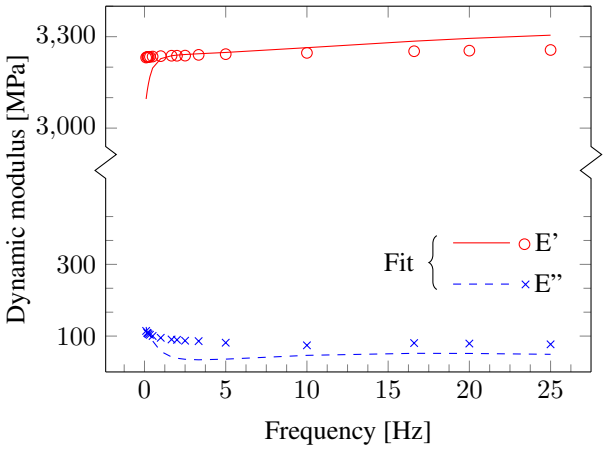

Figure 5: DMA results and least squares fit for dry samples.

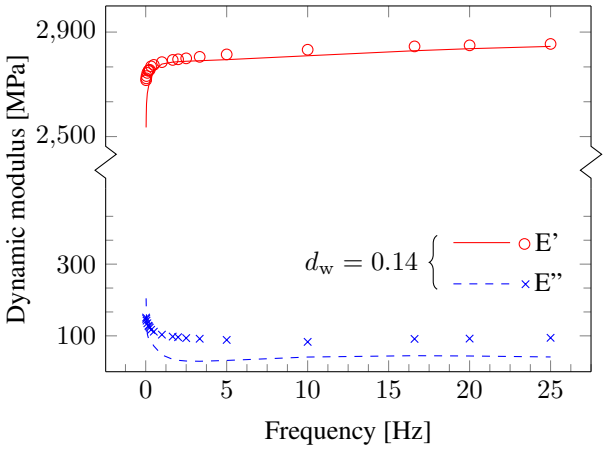

Figure 6: DMA results for saturated specimens and degraded dry response.

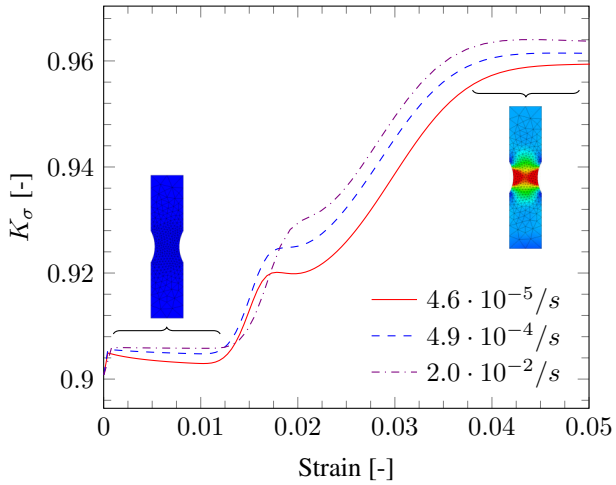

Figure 7: Evolution of stress concentration factor K_σ with strain for three different strain rates.

of the dog-bone was modeled and a stress concentration factor (K_σ) was computed in order to account for concentrations arising from the specimen geometry and the presence of grips:

$$K_\sigma = \frac{\sigma_y^{\text{num}} A}{F^{\text{num}}} \tag{48}$$

where A is the cross-sectional area at the center of the specimen and σ_y^{num} is the longitudinal stress at the same point resulting from the FE analysis when a prescribed displacement is applied to the top of the dog-bone and generates an internal force F_{num}. The experimental stress can then be estimated as:

$$\sigma_y^{\text{exp}} = K_\sigma \frac{F^{\text{exp}}}{A} \tag{49}$$

where F_{exp} is the force value measured by the load cell in the test frame.

The full dog-bone model was then substituted by a single-element model of the region where strain was measured. The experimental strain in the longitudinal direction was applied as a prescribed displacement and the fitting problem was cast as the minimization of the function:

$$f = \sum_t [\sigma_y^{\text{exp}}(t) - \sigma_y^{\text{num}}(t)]^2 \tag{50}$$

and solved using a nonlinear optimization algorithm.

In order to take into account the difference in yield behavior in tension and compression, a constant $\sigma_{\text{c}}/\sigma_{\text{t}}$ ratio of 1.25 was considered based on previously obtained experimental results [43]. Furthermore, since only longitudinal strains were used in the current calibration procedure, the value for $\nu_{\text{p}} = 0.32$ was also adopted from [43].

It is important to note that, due to the development of plastic strains at different rates for different parts of the specimen, K_σ is not constant but rather depends on the shape of the yield surfaces, the test speed and the current strain at the center of the specimen. Therefore, an iterative fitting procedure was performed: The experimental stresses were first obtained under the assumption of purely viscoelastic behavior. With the resultant VP properties, two additional calibration rounds were performed while updating the factors between each of them. Figure 7 shows the final stress concentration curves for the three different strain rates used for VP calibration as a function of strain at the center of the specimen.

Figure 8 shows the stress-strain curves obtained experimentally for each strain rate. Curves from different specimens tested in the same conditions exhibit low variability, similar to previous

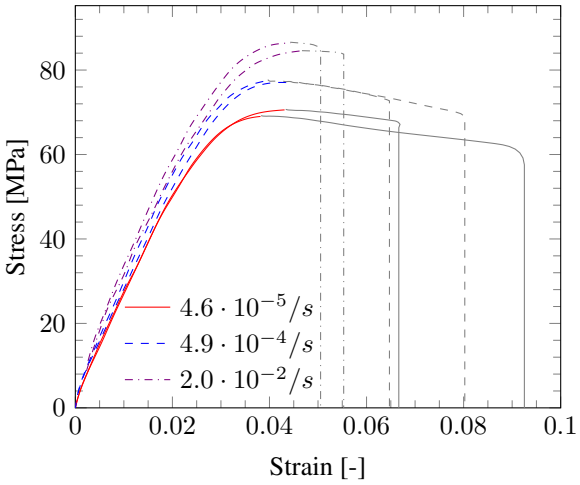

Figure 8: Experimental results for dry quasi-static tension in three different strain rates. Grayed lines indicate the response after strain localization.

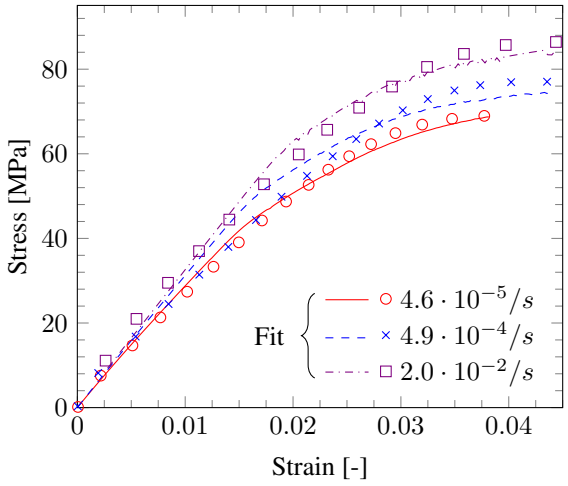

Figure 9: Fitted model response for dry quasi-static tension, with marks representing experimental results.

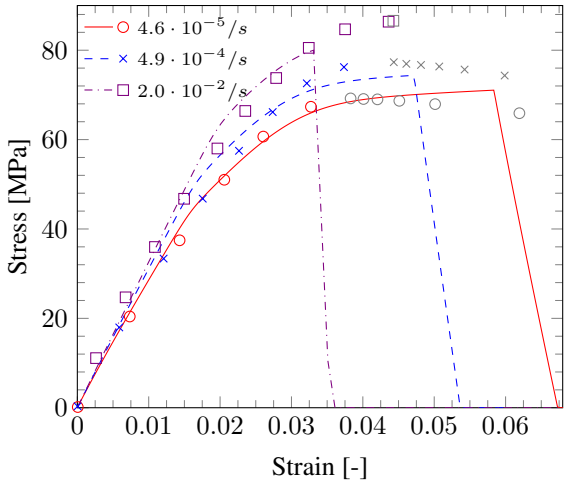

Figure 10: Model response of the dry material in tension including damage. Marks represent experimental results and gray marks indicate the response after strain localization.

observations in the same system [43] and suggesting that the performed tests have an acceptable degree of reproducibility. The portions of the curves depicted in gray refer to stress-train data obtained after the experimental load peak and were therefore not used for calibration since they may not represent the intrinsic constitutive behavior of the material [9]. As expected, the present epoxy system features nonlinear stress-strain behavior, in particular at strains higher than 0.02, exhibits strain-rate dependency and fractures at relatively low strain levels, with higher failure strains observed for slower tests.

Using a single curve for each strain rate, an exponential yield surface was fitted by determining the coefficients c_1 to c_5 in:

$$\sigma_{\mathrm{t}} = c_1 + c_2 \mathrm{e}^{\varepsilon^{\mathrm{p}}_{\mathrm{eq}}/c_3} + c_4 \mathrm{e}^{\varepsilon^{\mathrm{p}}_{\mathrm{eq}}/c_5} \tag{51}$$

as well as the VP parameters η_{p} and m_{p}, with the resultant properties shown in Table 1. Figure 9 shows the fitted curves together with their experimental counterparts. It can be seen that a good agreement was obtained for all rates, with only small deviations noted for the intermediate rate test at low strains.

3.3.3 Fracture

The first step in calibrating the damage model was fixing an upper bound for X_{t}, since rate dependency arises naturally as the material dissipates energy and the fracture surface shrinks. In view of the available test data, a pragmatic choice would be the peak load for the highest rate test (83.8 MPa). Naturally, bounding X_{t} in this manner will result in early failure for the highest strain rate test since the energy dissipation at the peak load would not be accounted for. Nevertheless, since failure occurs after the peak load for all strain rates, energy dissipation at the onset of fracture is not well defined and thus the practical choice of $X_{\mathrm{t}} = 83.8$ MPa was adopted.

With a value for X_{t}, the fracture energy $G^* = 1.9$ N/mm was computed using Eq. (37), leading to a vertical softening branch for $l_{\mathrm{e}} = 1.8\,mm$ failing at the upper bound of X_{t}. It is important to note that the sudden failure observed in the experiments is in fact a dynamic event for which part of the energy will be dissipated as kinetic energy. Since inertia effects are not taken into account in the energy expression of Eq. (21), the calibrated value of G^* should be interpreted with caution and cannot be seen as a fracture energy measurement.

The last step in the calibration process was the definition of X_{t} as a function of the accumulated dissipated energy measure Υ. As previously mentioned, the energy dissipation at failure is not

Viscoelasticity				
K_∞ [MPa]	3205			
G_∞ [MPa]	912			
K_r [MPa]	125	182	625	143
G_s [MPa]	36	52	178	41
k_r [s]	$4.16 \cdot 10^{-2}$	$2.30 \cdot 10^{0}$	$4.22 \cdot 10^{1}$	$3.11 \cdot 10^{4}$
g_s [s]	$1.46 \cdot 10^{-1}$	$8.08 \cdot 10^{0}$	$1.48 \cdot 10^{2}$	$1.09 \cdot 10^{5}$
Viscoplasticity				
σ_t [MPa]	$64.80 - 33.6\mathrm{e}^{-\epsilon^\mathrm{p}_\mathrm{eq}/0.003407} - 10.21\mathrm{e}^{-\epsilon^p_\mathrm{eq}/0.06493}$			
σ_c [MPa]	$81.0 - 42.0\mathrm{e}^{-\epsilon^\mathrm{p}_\mathrm{eq}/0.003407} - 12.77\mathrm{e}^{-\epsilon^p_\mathrm{eq}/0.06493}$			
η_p [s]	$3.49 \cdot 10^{12}$			
m_p [-]	7.305			
ν_p [-]	0.32			
Damage				
X_t [MPa]	$83.8 - 5.99\,\Upsilon$			
X_c [MPa]	$104.7 - 7.48\,\Upsilon$			
G^* [N/mm]	1.9			
Hygrothermal aging				
d_w^∞ [-]	0.14			
c_∞ [%]	3.2			

Table 1: Calibrated material properties.

well defined in quasi-static tests since it takes place after the global peak load and is therefore potentially influenced by strain localization and necking. The dissipation was therefore obtained from the stress-controlled fatigue test with the highest peak load (and thus the shortest duration). Since only one condition was used for calibration, a linear X_t decay was adopted:

$$X_\mathrm{t} = 83.8 - a\Upsilon \quad \text{with} \quad a = \frac{83.8 - \sigma_\mathrm{max}}{\Upsilon_\mathrm{break}} \tag{52}$$

where $\sigma_\mathrm{max} = 74.9$ MPa for the highest tested fatigue load and Υ_break was obtained by running the model for a number of load cycles equal to the average cycles at break obtained for the 3 specimens tested at this stress level.

The stress-strain response of the calibrated damage model can be seen in Figure 10. As expected, the failure strain for the curve with the highest strain rate was not correctly captured, which also caused the peak load to be slightly (approximately 2 MPa) lower. Failure for the other two strain rates occurred at higher strain levels, following the trend observed experimentally. It is interesting to note that since the adopted rheological model couples VE and VP ($\sigma_{ij}^\mathrm{hist}$ helps drive plastic strain development), the test with the highest strain ratio actually features a higher amount of plastic strain than the slower ones, leading to a higher energy dissipation and consequently to failure at a lower strain level.

3.4 Model predictions

In this section, the model is used to predict material behavior in loading scenarios not used for calibration, including quasi-static tensile tests of saturated specimens at different strain rates, loading-unloading tests with increasing strain amplitudes and stress-controlled fatigue tests. The predictions are compared with further experimental results and the model performance is discussed.

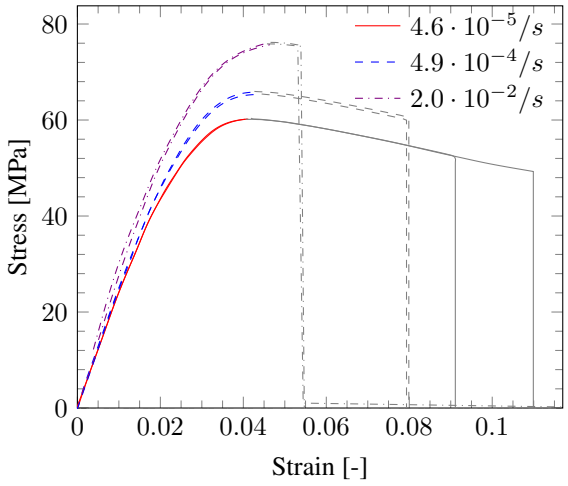

Figure 11: Tension results at different strain rates for saturated specimens. Grayed lines indicate the response after strain localization.

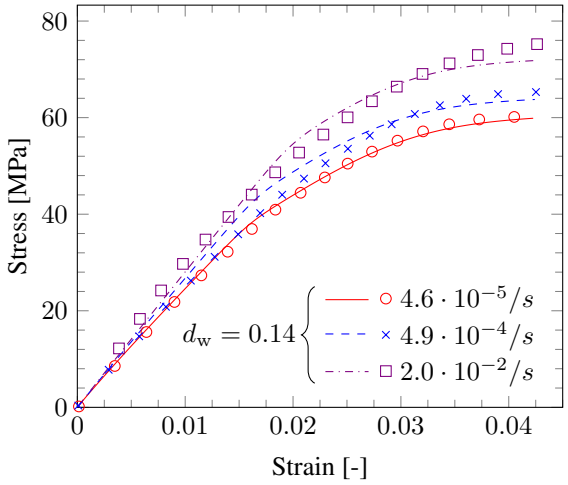

Figure 12: Saturated model results obtained by degrading the dry response. Marks represent experimental results on saturated specimens.

3.4.1 Water concentration influence

Figure 11 shows quasi-static tensile test results for specimens saturated in water at 50°C. Similar to dry specimens, results for all strain rates featured low scatter both in the elastic and plastic regimes as well as in the failure strain. Once again tests with the highest rate failed at higher stresses but lower strains, with only limited strain localization. Plasticization due to interaction with water molecules resulted in lower peak stresses for all rates. Interestingly enough, the failure strains remained similar to the ones from dry specimens, although it is difficult to determine the exact stress or strain at failure due to the occurrence of strain localization.

Using the dry VE/VP properties and the value for d_{w}^{∞} calibrated from DMA tests, the saturated VE/VP response was predicted and is shown together with the experimental pre-peak curves in Figure 12. The model shows excellent agreement with experiments for all strain rates, suggesting that the simple degradation model of Section 2.6 can effectively describe the behavior of the saturated resin in both VE and VP regimes, even though the viscoplastic parameters remain intact and only the backbone yield surface is degraded. Nevertheless, the present results are limited to quasi-static loading and further tests need to be performed in order to assess the performance of

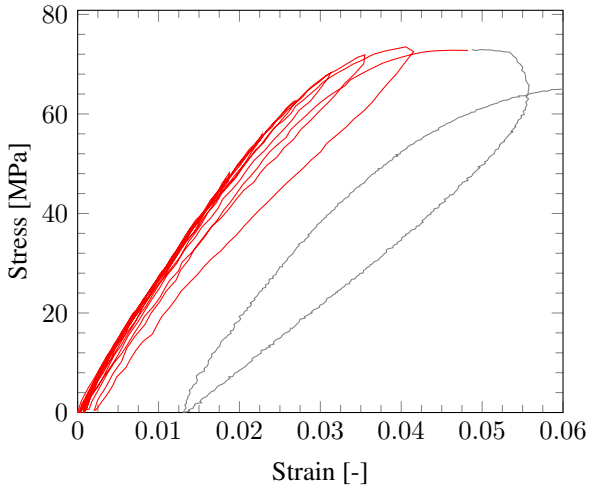

Figure 13: Experimental loading-unloading test with increasing amplitude (dry). Grayed lines indicate the response after strain localization.

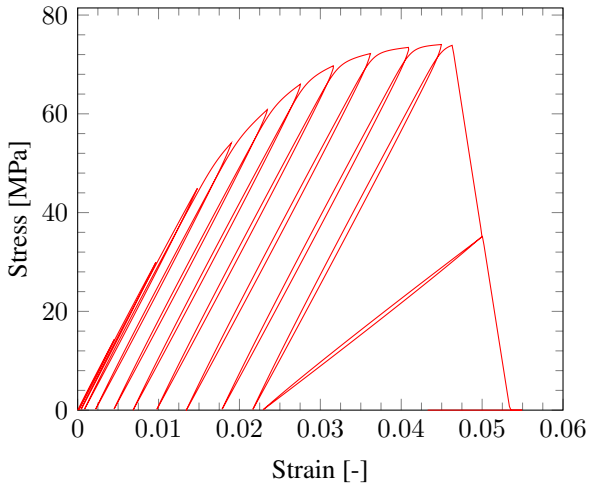

Figure 14: Numerical prediction of a loading-unloading test with increasing amplitudea (dry).

the model in predicting the fatigue behavior of saturated specimens.

3.4.2 Loading-unloading tests

The next loading scenario is a revisit of the loading-unloading test of Figure 1. Specimens were loaded in displacement control at 1 mm/min (strain rate of $4.9 \cdot 10^{-4}$/s) and unloaded at intermediate steps. A special test frame control procedure was then used in order to trigger a new loading phase when the force reached zero. Each loading cycle stopped at a linearly increasing maximum strain value until final failure. The resultant stress-strain curve can be seen in Figure 13 and the model prediction in Figure 14.

From the numerical response, it can be seen that all time-dependent phenomena mentioned in Section 1.1 are now present: Non-linear reloading branches that do not meet the original curve, hysteresis during unloading and failure at slightly lower strain and stress when compared to the monotonic response.

However, comparing the model prediction with the experimental curve makes an important shortcoming of the model evident. Even though the stresses at the unloading points are similar

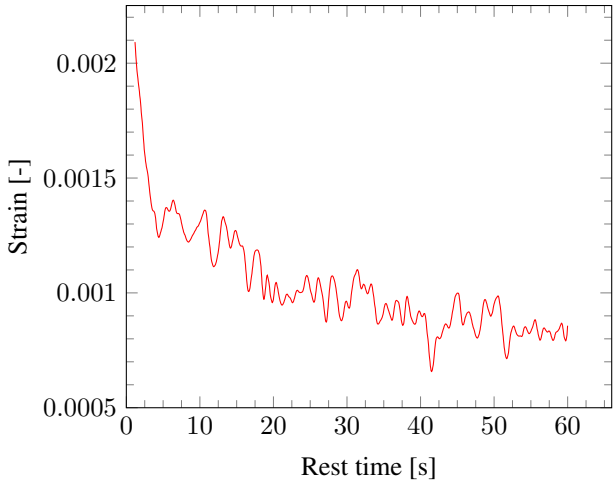

Figure 15: Strain relaxation after unloading from $\epsilon_{\text{amp}} = 0.035$, indicating the presence of permanent strains.

for the two curves, the model grossly overestimates the amount of plastic strain at the points of zero stress. The source of this discrepancy lies in the way by which the nonlinear part of the stress-strain response is modeled. While the load-displacement response of Figure 1 suggests the presence of significant pre-localization plastic strains, Figure 13 suggests that the greater part of the nonlinearity is in fact viscoelastic. This observation also helps to explain the differences in hysteresis area between model and experiments.

In order to confirm the existence of pre-localization plastic strains and rule out the possibility of a purely viscoelastic response, the same test was repeated but including rest periods of one minute at zero stress before reloading. Figure 15 shows the strain response obtained during one such rest period. Despite the presence of measurement noise, an asymptotic relaxation process towards a non-zero strain value can be clearly identified. It is concluded that the nonlinear behavior consists of a complex combination of nonlinear viscoelasticity and viscoplasticity.

It is important to note that either a purely VE model like the one proposed by Xia *et al.* [44] or the present VE/VP model are able to reproduce the quasi-static curves from the previous section, and the complex constitutive nature of the resin would be overlooked if no loading-unloading tests were performed. It is also interesting to note that even though the hysteresis area is underestimated by the model, the added plastic dissipation helps to diminish the difference in total dissipation and the damage part is activated at the same strain level at which localization starts in the experiments. Nevertheless, the inclusion of nonlinear viscoelasticity [44, 12] would improve the predictive capabilities of the present model.

3.4.3 Fatigue tests

The last loading scenario consists of stress-controlled fatigue tests at four different stress levels with an R-ratio ($\sigma_{\min}/\sigma_{\max}$) of 0.1 and a nominal strain rate of $2.0 \cdot 10^{-2}$/s. Since stress is controlled, VE creep and VP evolution become manifest in the form of ratcheting (*i.e.* strain accumulation with fatigue cycles). It is therefore interesting to track the evolution of strains at the peak and valley loads with the number of cycles. Figures 16 and 17 show strains at peak and valley stress, respectively, for the four stress levels, with lines representing model predictions. Since the model does not take into account the nonlinear viscoelastic behavior exhibited by the material, both peak and valley strains were overestimated. This overestimation is particularly significant for valley strains, similar to the mismatch in permanent strain observed in the loading-unloading

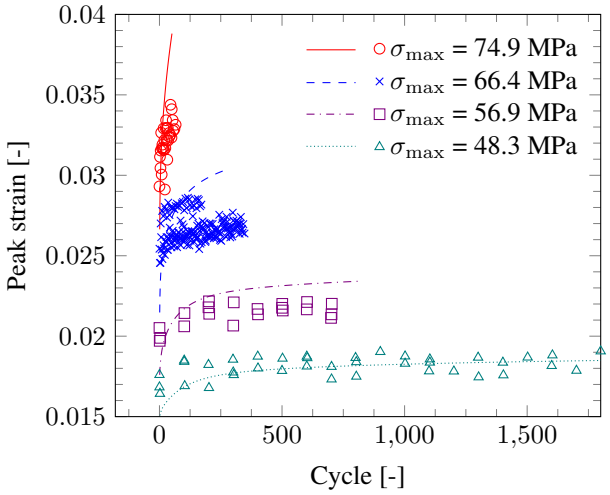

Figure 16: Experimental (marks) and numerical (lines) strains at peak loads for different load levels (dry).

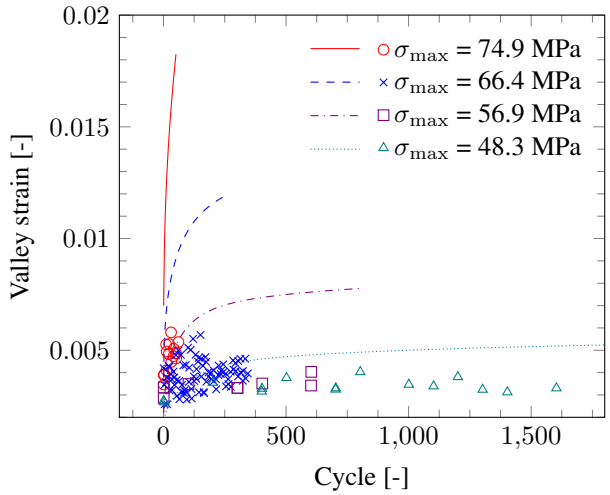

Figure 17: Experimental (marks) and numerical (lines) strains at valley loads for different load levels (dry).

tests. As $\sigma_{\max}$ decreases, the model predictions become more accurate because less plastic strain develops.

Figures 18 and 19 show experimental and numerical curves for a complete fatigue test with $\sigma_{\max} = 74.9$ MPa. The experimental response showed failure with no noticeable loss of stiffness and featured a large hysteresis area that is partly obscured by the ratcheting strain that develops with the number of cycles. The numerical response showed a significantly larger ratcheting strain, as the model relies on plastic strains in order to correctly represent the nonlinear stress-strain response.

Such differences in energy dissipation can be clearly seen in Figure 20, which shows stress-strain snapshots of a fatigue test at $\sigma_{\max} = 48.3$ MPa after 1300 load cycles, when the material is close to breaking. A large hysteresis loop can be seen in the experimental curve, while the numerically predicted area is significantly smaller. On the other hand, the model features a larger amount of viscoplastic dissipation, as evidenced by the higher valley strain. If the hypothesis that energy dissipation promotes initiation of fracture is valid, it is reasonable to suppose that

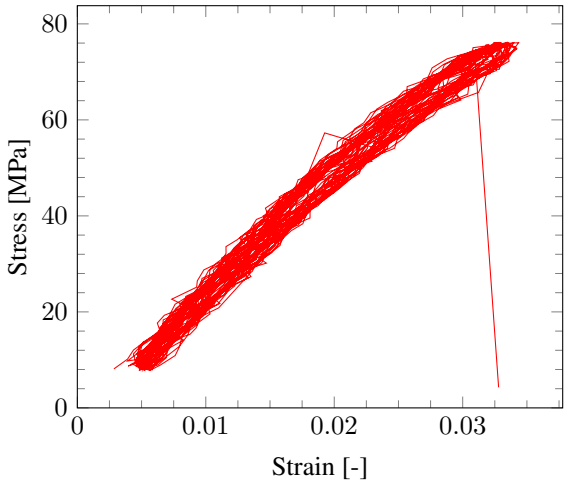

Figure 18: Experimental response in fatigue for $\sigma_{\max}$ = 74.9MPa (dry).

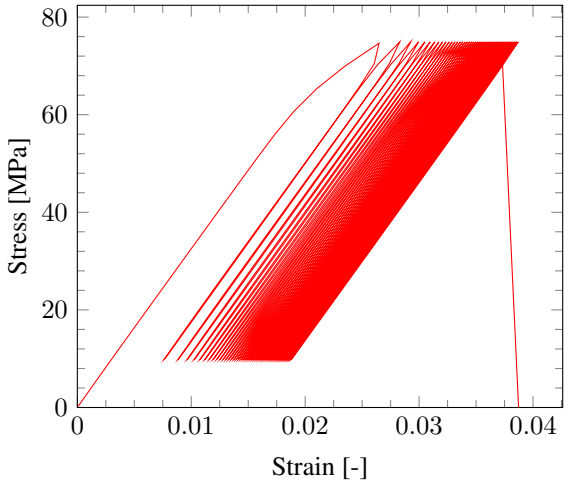

Figure 19: Numerical response in fatigue for $\sigma_{\max}$ = 74.9MPa (dry).

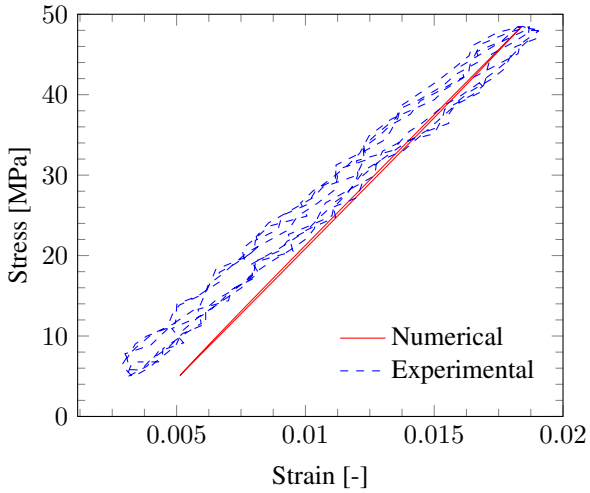

Figure 20: Dry material response after 1300 cycles with $\sigma_{\max} = 48.3$MPa.

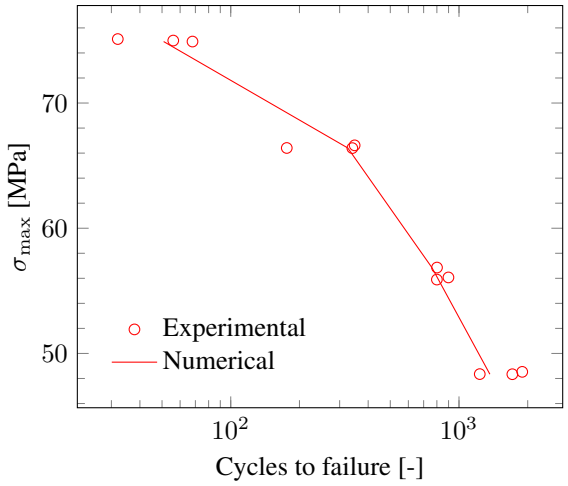

Figure 21: Experimental S/N curve and model prediction for dry specimens.

the erroneous viscoelastic dissipation predicted by the model will in part be compensated by its overestimated viscoplastic dissipation.

Using the fracture surface degradation calibrated with the tests at $\sigma_{\max} = 74.9$ MPa, the model was used to predict fatigue life at the three other stress levels, with results shown in Figure 21. The model gives reasonable estimates for the number of cycles to failure for all stress levels, suggesting that the dissipation-driven fracture initiation hypothesis is a valid approach for the high- to medium-cycle fatigue regimes. A loss of accuracy can be expected for lower stress levels as the viscoelastic dissipation will tend to dominate the material response and the present model is not able to reproduce this in a satisfactory manner. Furthermore, the role of dissipative mechanisms on fracture initiation might change in the high-cycle regime. More experimental data and model development are therefore necessary.

4 Conclusions

Based on preliminary experiments on an epoxy resin, a number of time-dependent phenomena were identified which are not taken into account by conventional elastoplastic models but may nevertheless play an important role in the long-term mechanical response of epoxy resins, such as hysteresis and strain-rate dependency. In this work, a viscoelastic/viscoplastic model with continuum damage was developed that can reproduce such phenomena.

The model consists of a parallel array of elastic Maxwell elements arranged in series with a pressure-dependent viscoplastic element. The integral viscoelastic stress update was presented in a time-discrete manner suitable for finite element implementation. For viscoplasticity, a Perzyna-type function was included in a non-associative plasticity model with general-shape yield functions. A pressure-dependent continuum damage model was developed for which the fracture surfaces are made to shrink as the material dissipates energy. Finally, a simple degradation model was presented for polymer degradation through plasticization.

The viscoelastic and viscoplastic properties were calibrated using DMA tests in bending and quasi-static monotonic tests in tension at different strain rates. The damage model was calibrated using static tests at a single strain rate and a short cyclic test with controlled stress. The calibrated model was able to accurately reproduce the rate-dependent material response both in plasticity and fracture, with good predictions for failure strain and maximum stress. The response of the water-saturated material at different rates was also predicted with excellent accuracy. For cyclic

tests, the model was found inadequate in its representation of the observed nonlinear stress-strain response which was modeled as plastic but is in fact a combination of plasticity and nonlinear viscoelasticity.

Acknowledgements

The authors acknowledge the contribution of the TKI-WoZ and IRPWIND projects for motivating and partly funding this research and of the TKI-MIMIC project industrial partners for providing useful feedback. The authors are also grateful to Catharina Visser, Frank Stroet and Luc Smissaert for the assistance provided in conducting the experimental campaign.

Declarations of interest

None.

A Derivative of the viscoplastic potential

The derivative of the viscoplastic potential of Eq. (20) with respect to $\Delta\gamma$ can be written as:

$$\frac{\partial \Phi}{\partial \Delta\gamma} = \frac{m_{\mathrm{p}} \Delta t}{\eta_{\mathrm{p}} \sigma_{\mathrm{t}}^0 \sigma_{\mathrm{c}}^0} \left(\frac{f_{\mathrm{p}}}{\sigma_{\mathrm{t}}^0 \sigma_{\mathrm{c}}^0} \right)^{m_{\mathrm{p}}-1} \frac{\partial f_{\mathrm{p}}}{\partial \Delta\gamma} - 1 = \widehat{V} \frac{\partial f_{\mathrm{p}}}{\partial \Delta\gamma} - 1 \tag{53}$$

where $\partial f / \partial \Delta\gamma$ is:

$$\frac{\partial f_{\mathrm{p}}}{\partial \Delta\gamma} = -\frac{72\widehat{G}}{\zeta_s^3} J_2^{\mathrm{tr}} - \frac{4\widehat{K}\alpha I_1^{\mathrm{tr}}}{\zeta_p^2}(\sigma_c - \sigma_t) + \frac{\partial f_{\mathrm{p}}}{\partial \varepsilon_{\mathrm{eq}}^{\mathrm{p}}} \frac{\partial \Delta\varepsilon_{\mathrm{eq}}^p}{\partial \Delta\gamma} \tag{54}$$

and $\partial f_{\mathrm{p}} / \partial \varepsilon_{\mathrm{eq}}^{\mathrm{p}}$ is:

$$\frac{\partial f_{\mathrm{p}}}{\partial \varepsilon_{\mathrm{eq}}^{\mathrm{p}}} = \frac{2I_1^{\mathrm{tr}}}{\zeta_p}(H_c - H_t) - 2(\sigma_c H_t + \sigma_t H_c) = \widehat{H} \tag{55}$$

where H_c and H_t are derivatives of σ_c and σ_t with respect to $\varepsilon_{\mathrm{eq}}^p$ and representing the compressive and tensile hardening moduli, respectively.

The only remaining term to compute in Eq. 54 is $\partial \Delta\varepsilon_{\mathrm{eq}}^p / \partial \Delta\gamma$. Substituting Eq. (14) in Eq. (13) and applying the trial stress conversion of Eq. (17), the variation of equivalent plastic strain becomes:

$$\Delta\varepsilon_{\mathrm{eq}}^p = \Delta\gamma \sqrt{\frac{\frac{18}{\zeta_s^2} J_2^{\mathrm{tr}} + \frac{4\alpha^2}{27\zeta_p^2}(I_1^{\mathrm{tr}})^2}{1 + 2\nu_p^2}} = \Delta\gamma \sqrt{\frac{\widehat{A}}{1 + 2\nu_p^2}} \tag{56}$$

and its derivative with respect to $\Delta\gamma$ is:

$$\frac{\partial \Delta\varepsilon_{\mathrm{eq}}^{\mathrm{p}}}{\partial \Delta\gamma} = \sqrt{\frac{1}{1 + 2\nu_{\mathrm{p}}^2}} \left[\sqrt{\widehat{A}} - \frac{\Delta\gamma}{2\sqrt{\widehat{A}}} \left(\frac{216\widehat{G} J_2^{\mathrm{tr}}}{\zeta_s^3} + \frac{16\alpha^3 \widehat{K} (I_1^{\mathrm{tr}})^2}{27\zeta_p^3} \right) \right] \tag{57}$$

B Viscoplastic tangent stiffness

Because of the time scale introduced by the viscous plastic multiplier of Eq. (16), there is no strict relationship between variations of stress and strain. However, since the stress update is

performed in a time discrete manner, it is still possible to define an algorithmic tangent matrix by differentiating Eq. (17) with respect to strain:

$$\frac{\partial \sigma_{ij}}{\partial \varepsilon_{kl}} = \frac{1}{\zeta_s}\frac{\partial S_{ij}^{\mathrm{tr}}}{\partial \varepsilon_{kl}} - \frac{6\widehat{G}}{\zeta_s^2} S_{ij}^{\mathrm{tr}} \frac{\partial \Delta\gamma}{\partial \varepsilon_{kl}} + \frac{1}{3\zeta_p}\delta_{ij}\frac{\partial I_1^{\mathrm{tr}}}{\partial \varepsilon_{kl}} - \frac{2\widehat{K}\alpha I_1^{\mathrm{tr}}}{3\zeta_p^2}\delta_{ij}\frac{\partial \Delta\gamma}{\partial \varepsilon_{kl}} \tag{58}$$

The derivatives of the deviatoric stress and first stress invariant can be readily computed:

$$\frac{\partial S_{ij}^{\mathrm{tr}}}{\partial \varepsilon_{kl}} = \widehat{G}\left(\delta_{ik}\delta_{jl} + \delta_{il}\delta_{jk} - \frac{2}{3}\delta_{ij}\delta_{kl}\right) \tag{59}$$

$$\frac{\partial I_1^{\mathrm{tr}}}{\partial \varepsilon_{kl}} = 3\widehat{K}\delta_{kl} \tag{60}$$

while the variation of the plastic multiplier with respect to strain is derived from differentiation of the viscoplastic consistency condition of Eq. (17) [2]:

$$\delta\Phi = \frac{\partial \Phi}{\partial \varepsilon_{kl}}\delta\varepsilon_{kl} + \frac{\partial \Phi}{\partial \Delta\gamma}\delta\Delta\gamma = 0 \quad \Rightarrow \quad \frac{\partial \Delta\gamma}{\partial \varepsilon_{kl}} = \frac{1}{\mu}\frac{\partial \Phi}{\partial \varepsilon_{kl}} \tag{61}$$

where μ is the negative of the derivative of Eq. (53):

$$\mu = -\frac{\partial \Phi}{\partial \Delta\gamma} \tag{62}$$

Differentiation of Φ with respect to strain takes a similar form as Eq. (53):

$$\frac{\partial \Phi}{\partial \varepsilon_{kl}} = \widehat{V}\frac{\partial f_{\mathrm{p}}}{\partial \varepsilon_{kl}} \tag{63}$$

and $\partial f_{\mathrm{p}}/\partial \varepsilon_{kl}$ in terms of trial stresses is given by:

$$\frac{\partial f_{\mathrm{p}}}{\partial \varepsilon_{kl}} = \frac{6}{\zeta_s^2}\frac{\partial J_2^{\mathrm{tr}}}{\partial \varepsilon_{kl}} + \frac{2(\sigma_c - \sigma_t)}{\zeta_p}\frac{\partial I_1^{\mathrm{tr}}}{\partial \varepsilon_{kl}} + \widehat{H}\frac{\partial \varepsilon_{\mathrm{eq}}^{\mathrm{p}}}{\partial \varepsilon_{kl}} \tag{64}$$

The derivative of the first invariant is shown in Eq. (60), while the derivative of J_2^{tr} is given by:

$$\frac{\partial J_2^{\mathrm{tr}}}{\partial \varepsilon_{kl}} = S_{ij}^{\mathrm{tr}}\frac{\partial S_{ij}^{\mathrm{tr}}}{\partial \varepsilon_{kl}} = 2\widehat{G}S_{kl}^{\mathrm{tr}} \tag{65}$$

The last term of Eq. (64) takes into account variations in yield stress with strain through the consequent variation in equivalent plastic strain [2]. The factor $\widehat{H}$ is given in Eq. (55), and $\partial \varepsilon_{\mathrm{eq}}^{\mathrm{p}}/\partial \varepsilon_{kl}$ is obtained from Eqs. (13) and (14):

$$\begin{aligned}\frac{\partial \varepsilon_{\mathrm{eq}}^{\mathrm{p}}}{\partial \varepsilon_{kl}} =& \frac{1}{1+2\nu_p^2}\frac{(\Delta\gamma)^2}{\Delta\varepsilon_{\mathrm{eq}}^{\mathrm{p}}}\left(\frac{3S_{ij}^{\mathrm{tr}}}{\zeta_s} + \frac{2\alpha I_1^{\mathrm{tr}}\delta_{ij}}{9\zeta_p}\right)\cdot \\ & \cdot\left(\frac{\widehat{G}}{\zeta_s}\big(3(\delta_{ik}\delta_{jl} + \delta_{il}\delta_{jk}) - 2\delta_{ij}\delta_{kl}\big) + \frac{2\widehat{K}\alpha}{3\zeta_p}\delta_{ij}\delta_{kl}\right) = \widehat{E}_{kl}\end{aligned} \tag{66}$$

Substitution of Eqs. (59), (60) and (61) in the tangent tensor of Eq. (58) yields:

$$\begin{aligned}\frac{\partial \sigma_{ij}}{\partial \varepsilon_{kl}} =& \frac{\widehat{G}}{\zeta_s}\left(\delta_{ik}\delta_{jl} + \delta_{il}\delta_{jk} - \frac{2}{3}\delta_{ij}\delta_{kl}\right) + \frac{\widehat{K}}{\zeta_p}\delta_{ij}\delta_{kl} \\ & - \frac{72\widehat{V}\widehat{G}^2}{\mu\zeta_s^4}S_{ij}^{\mathrm{tr}}S_{kl}^{\mathrm{tr}} - \frac{36(\sigma_c - \sigma_t)\widehat{V}\widehat{K}\widehat{G}}{\mu\zeta_p\zeta_s^2}S_{ij}^{\mathrm{tr}}\delta_{kl} \\ & - \frac{8\alpha I_1^{\mathrm{tr}}\widehat{V}\widehat{K}\widehat{G}}{\mu\zeta_p^2\zeta_s^2}\delta_{ij}S_{kl}^{\mathrm{tr}} - \frac{4\alpha I_1^{\mathrm{tr}}(\sigma_c - \sigma_t)\widehat{V}\widehat{K}^2}{\mu\zeta_p^3}\delta_{ij}\delta_{kl} \\ & - \frac{6\widehat{V}\widehat{G}\widehat{H}}{\mu\zeta_s^2}S_{ij}^{\mathrm{tr}}\widehat{E}_{kl} - \frac{2\alpha I_1^{\mathrm{tr}}\widehat{V}\widehat{K}\widehat{H}}{3\mu\zeta_p^2}\delta_{ij}\widehat{E}_{kl}\end{aligned} \tag{67}$$

which can be cast in the notation adopted by Melro *et al*. [1] and later by Van der Meer [2]:

$$\frac{\partial \boldsymbol{\sigma}}{\partial \boldsymbol{\varepsilon}} = \beta \mathbf{I}_4^s + \left(\phi - \frac{\beta}{3}\right)\mathbf{II} - \rho \mathbf{S}^{\mathrm{tr}}\mathbf{I} - \chi \mathbf{S}^{\mathrm{tr}}\mathbf{S}^{\mathrm{tr}} - \psi \mathbf{I}\mathbf{S}^{\mathrm{tr}} - \omega \mathbf{S}^{\mathrm{tr}}\mathbf{E} - \xi \mathbf{I}\mathbf{E} \tag{68}$$

where $\mathbf{I}_4^s = 1/2(\delta_{ik}\delta_{jl} + \delta_{il}\delta_{jk})$ and the coefficients are given by:

$$\beta = \frac{2\widehat{G}}{\zeta_s} \quad \phi = \frac{\widehat{K}}{\zeta_p} - \frac{4\alpha I_1^{\mathrm{tr}}(\sigma_c - \sigma_t)\widehat{V}\widehat{K}^2}{\mu \zeta_p^3} \tag{69}$$

$$\rho = \frac{36(\sigma_c - \sigma_t)\widehat{V}\widehat{K}\widehat{G}}{\mu \zeta_p \zeta_s^2} \quad \chi = \frac{72\widehat{V}\widehat{G}^2}{\mu \zeta_s^4} \tag{70}$$

$$\psi = \frac{8\alpha I_1^{\mathrm{tr}}\widehat{V}\widehat{K}\widehat{G}}{\mu \zeta_p^2 \zeta_s^2} \quad \omega = \frac{6\widehat{V}\widehat{G}\widehat{H}}{\mu \zeta_s^2} \quad \xi = \frac{2\alpha I_1^{\mathrm{tr}}\widehat{V}\widehat{K}\widehat{H}}{3\mu \zeta_p^2} \tag{71}$$

C Damage tangent stiffness

Since plasticity is deactivated after damage starts, the total strain rate is fully elastic (*i.e.* $\dot{\varepsilon}_{kl} = \dot{\varepsilon}^{\mathrm{e}}_{kl}$) and differentiation of Eq. (29) yields:

$$\frac{\partial \sigma_{ij}}{\partial \varepsilon_{kl}} = (1-d)\frac{\partial \widetilde{\sigma}_{ij}}{\partial \varepsilon^{\mathrm{e}}_{kl}} - \frac{\partial d}{\partial r}\widetilde{\sigma}_{ij}\frac{\partial r}{\partial \varepsilon^{\mathrm{e}}_{kl}} \tag{72}$$

which can be cast in a form similar to Eq. (68):

$$\frac{\partial \boldsymbol{\sigma}}{\partial \boldsymbol{\varepsilon}} = \beta \mathbf{I}_4^s + \left(\phi - \frac{\beta}{3}\right)\mathbf{II} - \rho \widetilde{\mathbf{S}}\mathbf{I} - \chi \widetilde{\mathbf{S}}\widetilde{\mathbf{S}} - \psi \mathbf{I}\widetilde{\mathbf{S}} \tag{73}$$

with coefficients:

$$\beta = 2(1-d)\widehat{G} \quad \phi = (1-d)\widehat{K} - \frac{\widehat{D}\widehat{K}\widetilde{I}_1(X_{\mathrm{c}} - X_{\mathrm{t}})}{X_{\mathrm{c}}X_{\mathrm{t}}} \tag{74}$$

$$\rho = \frac{3\widehat{D}\widehat{K}(X_{\mathrm{c}} - X_{\mathrm{t}})}{X_{\mathrm{c}}X_{\mathrm{t}}} \quad \chi = \frac{6\widehat{D}\widehat{G}}{X_{\mathrm{c}}X_{\mathrm{t}}} \quad \psi = \frac{2\widehat{D}\widehat{G}\widetilde{I}_1}{X_{\mathrm{c}}X_{\mathrm{t}}} \tag{75}$$

where $\widehat{K} = K_\infty + K_{\mathrm{ve}}(\Delta t)$, $\widehat{G} = G_\infty + G_{\mathrm{ve}}(\Delta t)$ and $\widehat{D} = \partial d/\partial r$.

References

References

[1] A. R. Melro, P. P. Camanho, F. M. Andrade Pires, S. T. Pinho, Micromechanical analysis of polymer composites reinforced by unidirectional fibres: Part I - Constitutive modelling, International Journal of Solids and Structures 50 (2013) 1897–1905.

[2] F. P. van der Meer, Micromechanical validation of a mesomodel for plasticity in composites, European Journal of Mechanics - A/Solids 60 (2016) 58–69.

[3] F. Naya, C. González, C. S. Lopes, S. van der Veen, F. Pons, Computational micromechanics of the transverse and shear behaviour of unidirectional fiber reinforced polymers including environmental effects, Composites Part A - Applied Science and Manufacturing 92 (2016) 146–157.

[4] K. Terada, M. Kurumatani, Two-scale diffusion-deformation coupling model for material deterioration involving micro-crack propagation, International Journal for Numerical Methods in Engineering 83 (2010) 426–451.

[5] E. Kontou, Viscoplastic deformation of an epoxy resin at elevated temperatures, Journal of Applied Polymer Science 101 (2006) 2027–2033.

[6] G. Tao, Z. Xia, Ratcheting behavior of an epoxy polymer and its effect on fatigue life, Polymer Testing 26 (2007) 451–460.

[7] G. Tao, Z. Xia, Mean stress/strain effect on fatigue behavior of an epoxy resin, International Journal of Fatigue 29 (2007) 2180–2190.

[8] B. Fiedler, M. Hojo, S. Ochiai, K. Schulte, M. Ando, Failure behavior of an epoxy matrix under different kinds of static loading, Composites Science and Technology 61 (2001) 1615–1624.

[9] X. Poulain, A. A. Benzerga, R. K. Goldberg, Finite-strain elasto-viscoplastic behavior of an epoxy resin: Experiments and modeling in the glassy regime, International Journal of Plasticity 62 (2014) 138–161.

[10] A. Krairi, I. Doghri, A thermodynamically-based constitutive model for thermoplastic polymers coupling viscoelasticity, viscoplasticity and ductile damage, International Journal of Plasticity 60 (2014) 163–181.

[11] M. N. Silberstein, M. C. Boyce, Constitutive modeling of the rate, temperature, and hydration dependent deformation response of nafion to monotonic and cyclic loading, Journal of Power Sources 195 (2010) 5692–5706.

[12] C. Yu, G. Kang, K. Chen, A hygro-thermal-mechanical coupled cyclic constitutive model for polymers with considering glass transition, International Journal of Plasticity 89 (2017) 29–65.

[13] G. M. Odegard, A. Bandyopadhyay, Physical aging of epoxy polymers and their composites, Journal of Polymer Science: Part B: Polymer Physics 49 (2011) 1695–1716.

[14] R. Polanský, V. Mantlík, P. Prosr, J. Sušír, Influence of thermal treatment on the glass transition temperature of thermosetting epoxy laminate, Polymer Testing 28 (2009) 428–436.

[15] X. Bai, M. A. Bessa, A. R. Melro, P. P. Camanho, L. Guo, W. K. Liu, High-fidelity micro-scale modeling of the thermo-visco-plastic behavior of carbon fiber polymer matrix composites, Composite Structures 134 (2015) 132–141.

[16] S. Haouala, I. Doghri, Modeling and algorithms for two-scale time homogenization of viscoelastic-viscoplastic solids under large numbers of cycles, International Journal of Plasticity 70 (2015) 98–125.

[17] C. Yu, G. Kang, F. Lu, Y. Zhu, C. K., Viscoelastic-viscoplastic cyclic deformation of polycarbonate polymer: experiment and constitutive model, Journal of Applied Mechanics 83 (2016) 1–14.

[18] H. Zhu, L. Sun, A viscoelastic-viscoplastic damage constitutive model for asphalt mixtures based on thermodynamics, International Journal of Plasticity 40 (2002) 81–100.

[19] H. J. Eyring, Viscosity, plasticity, and diffusion as examples of absolute reaction rates, The Journal of Chemical Physics 4 (1936) 283–291.

[20] T. A. Tervoort, E. T. J. Klompen, L. E. Govaert, A constitutive equation for the elasto-viscoplastic deformation of glassy polymers, Journal of Rheology 40 (1996) 779–797.

[21] T. A. Tervoort, R. J. M. Smit, W. A. M. Brekelmans, L. E. Govaert, A constitutive equation for the elasto-viscoplastic deformation of glassy polymers, Mechanics of Time-Dependent Materials 1 (1998) 269–291.

[22] L. E. Govaert, H. J. Schellens, H. J. M. Thomassen, R. J. M. Smit, L. Terzoli, T. Peijs, A micromechanical approach to time-dependent failure in off-axis loaded polymer composites, Composites Part A - Applied Science and Manufacturing 32 (2001) 1697–1711.

[23] A. S. Argon, A theory for the low-temperature plastic deformation of glassy polymers, Philosophical Magazine 28 (1973) 839–865.

[24] M. C. Boyce, E. M. Arruda, Constitutive models of rubber elasticity: A review, Rubber Chemistry and Technology 73 (2000) 504–523.

[25] E. van der Giessen, Localized plastic deformations in glassy polymers, European Journal of Mechanics - A/Solids 16 (1997) 87,106.

[26] L. Anand, N. M. Ames, V. Srivastava, S. A. Chester, A thermo-mechanically coupled theory for large deformations of amorphous polymers. Part I: Formulation, International Journal of Plasticity 25 (2009) 1474–1494.

[27] J. L. Bouvard, D. K. Francis, M. A. Tschopp, E. B. Marin, D. J. Bammann, M. F. Horstemeyer, An internal state variable material model for predicting the time, thermomechanical, and stress state dependence of amorphous glassy polymers under large deformation, International Journal of Plasticity 42 (2013) 168–193.

[28] A. D. Drozdov, J. C. Christiansen, Viscoelasticity and viscoplasticity of semicrystalline polymers: Structure-property relations for high-density polyethylene, Computational Materials Science 39 (2007) 729–751.

[29] A. D. Drozdov, Cyclic viscoelastoplasticity and low-cycle fatigue of polymer composites, International Journal of Solids and Structures 48 (2011) 2026,2040.

[30] A. D. Drozdov, Multi-cycle viscoplastic deformation of polypropylene, Computational Materials Science 50 (2011) 1991–2000.

[31] C. Miehe, S. Göktepe, J. Méndez Diez, Finite viscoplasticity of amorphous glassy polymers in the logarithmic strain space, International Journal of Solids and Structures 46 (2009) 181–202.

[32] S. Kweon, A. A. Benzerga, Finite element implementation of a macromolecular viscoplastic polymer model, International Journal for Numerical Methods in Engineering 94 (2013) 895–919.

[33] C. Oskay, J. Fish, Fatigue life prediction using 2-scale temporal asymptotic homogenization, International Journal for Numerical Methods in Engineering 61 (2004) 329–359.

[34] R. Crouch, C. Oskay, J. Fish, Multiple spatio-temporal scale modeling of composites subjected to cyclic loading, Computational Mechanics 51 (2013) 93–107.

[35] J. C. Simo, J. W. Ju, Strain- and stress-based continuum damage models - I. Formulation, International Journal of Solids and Structures 23 (1987) 821–840.

[36] J. Lemaitre, Coupled elasto-plasticity and damage constituive equations, Computer Methods in Applied Mechanics and Engineering 51 (1985) 31–49.

[37] A. Arefi, F. P. van der Meer, Formulation of a consistent pressure-dependent damage model with fracture energy as input, Composite Structures 201 (2018) 208–216.

[38] Z. P. Bažant, B. Oh, Crack band theory for fracture of concrete, Materials and Structures 16 (1983) 155–177.

[39] P. Davies, F. Mazéas, P. Casari, Sea water aging of glass reinforced composites: Shear behaviour and damage modelling, Journal of Composite Materials 35 (15) (2000) 1343–1372.

[40] I. B. C. M. Rocha, S. Raijmaekers, R. P. L. Nijssen, F. P. van der Meer, L. J. Sluys, Hygrothermal ageing behaviour of a glass/epoxy composite used in wind turbine blades, Composite Structures 174 (2017) 110–122.

[41] B. Miled, Coupled viscoelastic-viscoplastic modeling of homogeneous and reinforced thermoplastic polymers, PhD thesis, Université Catholique de Louvain, 2011.

[42] Jive - Software development kit for advanced numerical simulations, http://jive.dynaflow.com, accessed: 18-12-2017.

[43] I. B. C. M. Rocha, F. P. van der Meer, R. P. L. Nijssen, L. J. Sluys, A multiscale and multiphysics numerical framework for modelling of hygrothermal ageing in laminated composites, International Journal for Numerical Methods in Engineering 112 (2017) 360–379.

[44] Z. Xia, Y. Hu, F. Ellyin, Deformation behavior of an epoxy resin subject to multiaxial loadings. Part ii: Constitutive modeling and predictions, Polymer Engineering and Science 43 (2003) 734–748.